NOAA/SEC SXI-M INSTRUMENT ANALYSIS REPORT

DETECTOR SENSITIVITY

V. J. Pizzo, 20/04/99

1. Purpose

This report addresses the SXI-M detector sensitivity in the integrated-counting mode. It builds upon and supersedes the findings presented in Section 6 of the "Interim Report on SXI Sensitivity Analysis", compiled 8/21/96 by V. J. Pizzo. It makes use of findings in the MSFC report on the "Integrated X-ray Sensitivity Characterization of the SXI Flight Detector" (K. Russell and J. Chappell, April 13, 1997), and relates results of this study to MSFC results where possible.

2. Data Input

The analysis described herein is based upon the detector sensitivity tests run 96/10/20 (aluminum source, "Al", 8.3Å) and 96/10/22 (carbon source, "C", 44.7Å). The test setup and procedure is described fully in Secs 1-3 of the MSFC document referenced above and in "SXI Flight Detector Sensitivity Characterization Test Procedure", MSFC MTCP-FC-SXI-055, by E. Corder, J. Briscoe, and K. Russell. This analysis makes use of the same images as the MSFC study (with a few inconsequential exceptions), and the parameters for the absolute calibration and the derived fluxes measured by the flow meter are essentially identical. Hence discrepancies between the two studies derive mainly from differences in the following elements of the data reduction:

1) background determination and subtraction
2) implementation of fit scheme (eg, semi-log vs log-log, treatment of statistical outliers, etc.)

3. Data Reduction

The data used in the analysis are tabulated in Appendix 1 and 2, and the analysis is conducted according to the following scheme:

1) Determine the SXI detector background
    a) The zero-voltage MCP background images with x-ray source on are read in and segregated by integration time. Note that two each of images at 8, 15, 30, and 60s duration were taken at the start of the run for each source, and a single image at each integration time was taken for reference at the end of each run.
    b) A region of interest (ROI) is defined and the average DN per pixel and standard deviations are computed for the same ROI in each image in the entire analysis. The primary ROI was a 256×256 box centered on the middle of the CCD; other ROIs were considered in the analysis, as described below. Line-by-line background subtraction is not necessary, since in this case we are

averaging over an ROI wherein the input flux is approximately uniform over areas large by comparison with pixel dimensions. (The MSFC document "Flat Field Analysis for the SXI Flight Detector", by K. Russell and J. Chappell, 5/1/97, concludes that the detector response with the Al beam was uniform to about 3%; see their Fig 2. Some vignetting of the source beam near the corners of the CCD is noted.) Likewise, voltage line droop effects and flat-field corrections are not applied, since in all images the same ROI is considered and it is the signal above background that we are interested in.

c) A straight line is fit to the background average values, as a function of integration time. The resulting zero-integration-time intercept (C_1) is equivalent to the "ADC offset" value described in the MSFC Integrated Sensitivity document, and the slope (C_2) corresponds to their "non x-ray" (time-dependent) component of the background signal. The very fact that there is an increase in mean DN with time indicates that the reference pixel methodology adopted for the SXI detector does not provide adequate background subtraction; the reference pixel evidently builds up noise at a different rate than the rest of the pixels in the row.

Figs. 1a-b show the background DN in the ROI as a function of integration time for both Al and C sources. For aluminum, exposures taken at the start and end of the run show consistent mean DN; hence the straight line fit shown by the solid line is used for the background correction for the Al images. (See Table 1 for a listing of background fit parameters used in the analysis.)

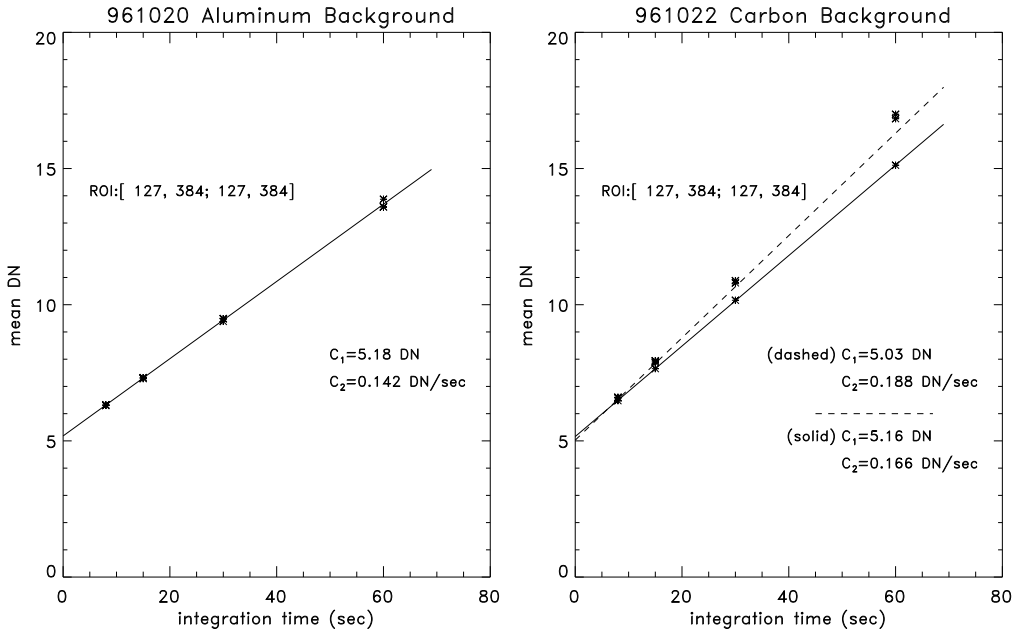

Fig. 1. Variation of mean background with time for the Al and C data sets.

For C, the background drifted noticeably between the start and the end of the test. The dashed line in Fig 1b shows the fit to all the background C images. However,

the uppermost asterisks in the plot show the mean DN from images at the start of the run, while the lower set (denoted by the solid line) come from images taken at the end of the run, some nine hours later. The drift in the background affects the longest exposures most. This poses a major problem for the C analysis, since the source is intrinsically weaker and longer exposures were used to obtain the necessary statistics. While it is not possible to say how fast the background drift occurred, note that even during the first set of background images, each successive image at the same exposure invariably shows less DN than the preceding one (see data listings in Appendix 2). We therefore speculate that the background drift is a thermal effect, with most of the adjustment taking place near the start of the test run. (Note that the lowest voltage images are taken early in the test run and would therefore be most affected by the background drift.) Hence we adopt the solid line fit to the lower set of points as the correct background. The corresponding fit parameters are listed in Table 1.

Table 1. Background Fit Parameters

	C_1 (DN)	C_2 (DN/sec)
Al	5.18	0.142
C	5.16	0.166

2) Obtain average DN in images with MCP at operating voltages

   a) Using the same ROI as for the background images, obtain the raw average DN ($\overline{\mathrm{DN}}$) per pixel and standard deviation (SDN) for each image. These cover a range of MCP voltages from 570V to 990V and integration times from .25s to 60s.
   b) Sort according to MCP voltage and integration time.

3) Determine incident photon flux

   From flow meter data (*.spm files), compute incident photon flux per pixel (I_p) appropriate for each integration time. In this, we follow the MSFC Integrated Sensitivity document closely, and the differences in values are negligible. The main sources of error in the flow meter estimates are the background correction, the precision of the flow meter alignment and location with respect to the source, and brehmstrahlung continuum contamination falling within the finite width of the source filter bandpass.

4) Determine detector response as function of incident photon flux

   Fig. 2 presents the mean DN/pixel response as a function of photon flux. Each asterisk in the plot refers to an individual image. At high DN and photon flux the response is quite linear, but at low DN and photon flux the background contribution causes the curves to flatten out.

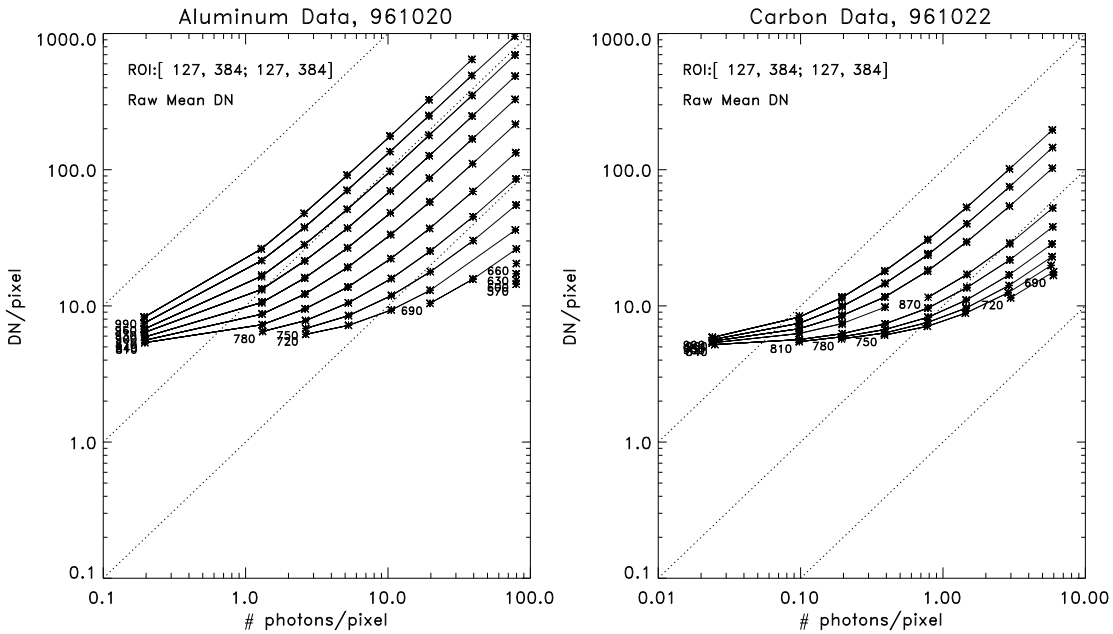

Fig. 2. Integrated DN per pixel as function of incident photon flux, no background correction.

5) Correct for detector background

   a) Using the background fit parameters derived above, subtract from each image the appropriate background DN to obtain the background-corrected DN per pixel (CDN). Thus,

$$\mathrm{CDN} = \overline{\mathrm{DN}} - \mathrm{C}_1 - (\mathrm{integration\,time} * \mathrm{C}_2)$$

Fig. 3 shows the background-corrected (CDN) response for Al and C. In both cases, the response is a very linear function of incident photon flux, except where both incident photon fluxes and CDN are quite low. This gives confidence that the background correction has been handled adequately, particularly in view of the large corrections required at low $\overline{\mathrm{DN}}$ and low photon fluxes. (Compare Figs. 2 and 3.) Figs. 3*ab* suggest the detector responds linearly over a dynamic range of at least 300 in both CDN and photon flux.

6) From the CDN and I_p, compute the detector sensitivity as:

$$\overline{\mathrm{S}} = \mathrm{CDN}/\mathrm{I_p}$$

N.B.: The units of $\overline{\mathrm{S}}$ are DN per photon incident on the MCP face.

Fig. 4 shows log-log plots of $\overline{\mathrm{S}}$ data for all useful Al and C images as a function of MCP voltage. At each voltage, the overstriking "*" symbols denote individual

images taken at that voltage but with different integration times. While the overall trend is roughly linear in both plots (implying a power-law relation between $\overline{S}$ and MCP voltage), a fair amount of scatter is evident at each voltage setting.

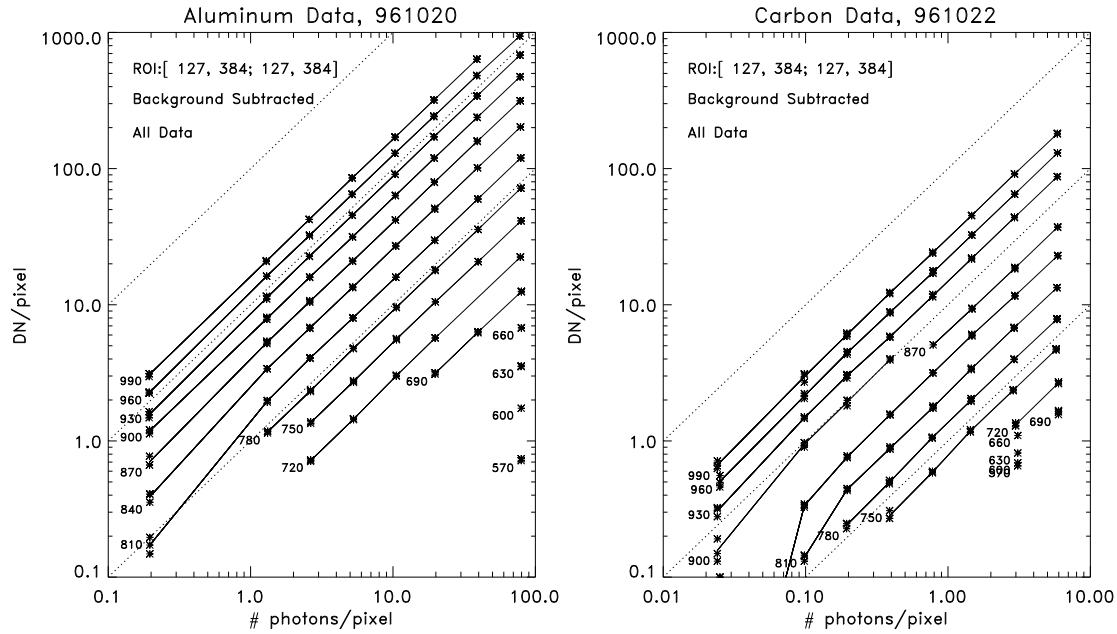

Fig. 3. Same as Fig. 2, background correction included (CDN).

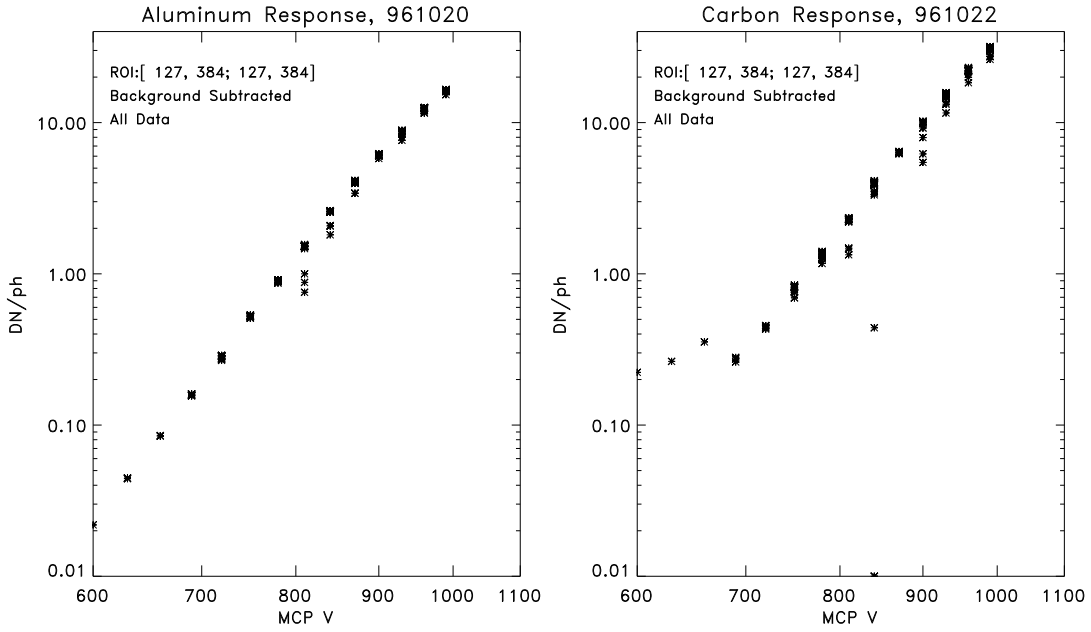

Fig. 4. Log-log plot of detector CDN/photon response as function of MCP voltage.

7) Obtain a good fit to the quantity CDN/I_p versus MCP voltage; relate Aluminum 8.3Å results to Carbon 44Å results.

Much of the scatter at each voltage setting in Fig. 4 stems from images taken with the shortest integration times; these have very low CDN and low statistical accuracy. It is therefore appropriate to eliminate all those points for which CDN $<$ SDN before functional fitting is attempted. The result of this screening process is seen in Fig. 5. The remaining CDN are extremely linear with incident photon flux, albeit over a shorter range of values.

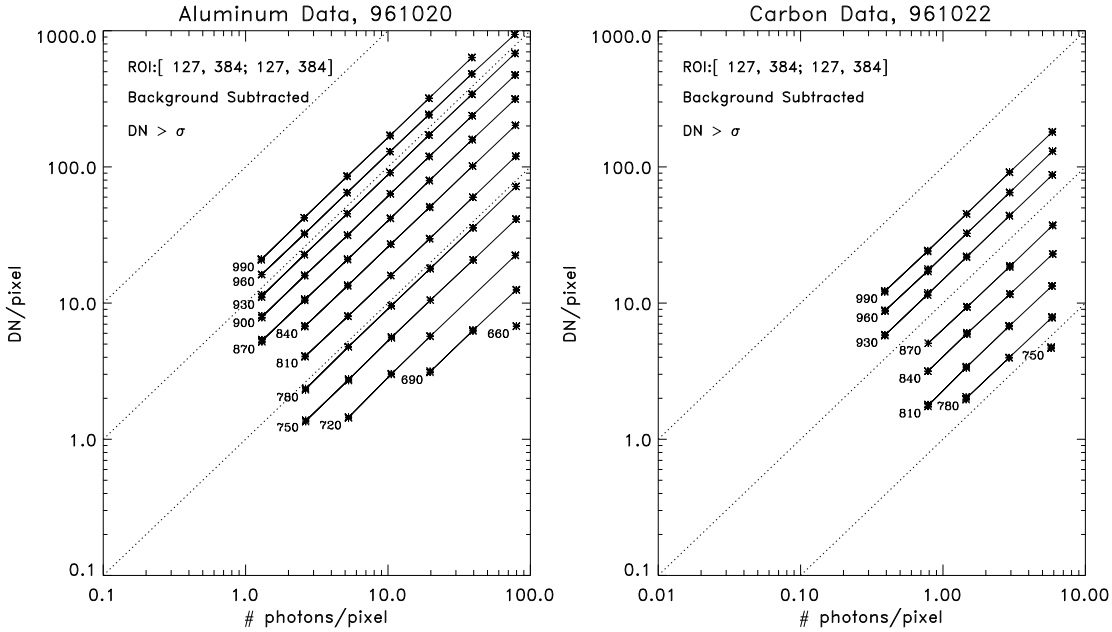

Fig. 5. Same as Fig. 3, low accuracy data excluded.

Fig. 6 shows the screened $\overline{S}$ values as a function of MCP voltage, plotted in log-log space. Least-squares fits using standard techniques (assuming equal weighting) are given by the straight lines. The fits may be expressed as power laws of the form

$$\mathrm{DN/ph} = \mathrm{A} * (\mathrm{MCP}/1000)^{\mathrm{B}}$$

where the constants A and B are given by:

$$\mathrm{A} = 30.65 \pm 1.18\,\mathrm{DN/ph}, \quad \mathrm{B} = 14.20 \pm 0.02 \qquad [\mathrm{Al}]$$

$$\mathrm{A} = 46.64 \pm 2.19\,\mathrm{DN/ph}, \quad \mathrm{B} = 14.20 \pm 0.12 \qquad [\mathrm{C}]$$

and MCP is the requested voltage. These fits were derived from the data for which MCP $<$ 850V, where the dependence appears most linear. This regime also coincides with the anticipated prime operational voltage range for the MCP. Above 850V, there is a definite roll-off in response for both Al and C, which may be indicative of detector saturation. (See Section 4.5 below for a discussion of saturation effects.)

The linearity of the fit below 850V is striking, and the same slope is derived for both Al and C. It is to be stressed that the agreement in slope values was not

imposed on the analysis, but was derived from it. This is just what is expected on physical grounds, but had not been confirmed in the MSFC analysis or in preliminary SEC analyses. In addition, the C/Al response ratio is 1.52, which is very near the expected value of 1.5, based upon known quantum efficiencies for the MCP glass strata (∼12% at C, ∼8% at Al.)

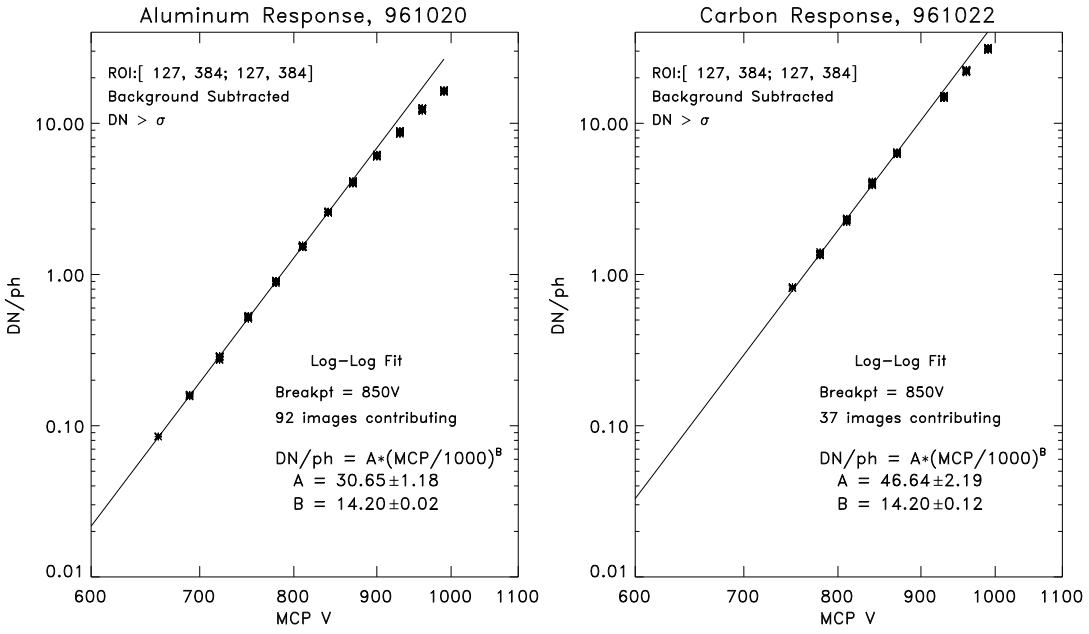

Fig. 6. Power-law fit to $\overline{S}$ data for which MCP voltage < 850V.

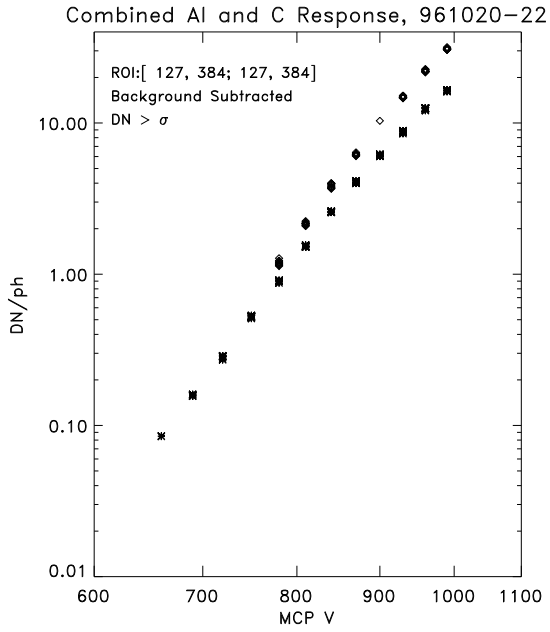

Fig. 7. Overlay of Al data ("*") from Fig. 6 with C data (diamonds) processed with background correction derived from background images taken at start of test run.

The inconsistency in slope for Al and C encountered in previous studies (e.g., the MSFC analysis, the preliminary SEC analysis) is attributed to the apparent temporal drift in background in the C data, which is now accounted for. Further support for this view may be found in Fig. 7, which shows an overlay of Al and C values for CDN/I_p versus MCP voltage. In this case, the background for C was given by the upper (dashed) line in Fig. 1b, which was derived from background images taken at the start of the test series. The discordant slopes visible here are removed when the proper background is used (cf. Fig. 6).

4. Additional Considerations

Several issues remain to be addressed.

1) Log-log fitting versus semi-log or other form.

There is no compelling physical reason for using a log-log fit to characterize the mean DN per photon response as a function of MCP voltage; it seems to describe the data in the primary range of interest (MCP $\lesssim$ 900V) quite adequately, and it yields a convenient expression for the response. To assess the merits of other fits, we compare in Fig. 8 a semi-log fit (as used in the MSFC Integrated Sensitivity analysis) to the same data as in Fig. 6. The roll-off at the upper end seems more pronounced than in the log-log fit, and there is a hint of roll-off at the lower end in Al. We conclude there is nothing obvious to be gained from a semi-log fit.

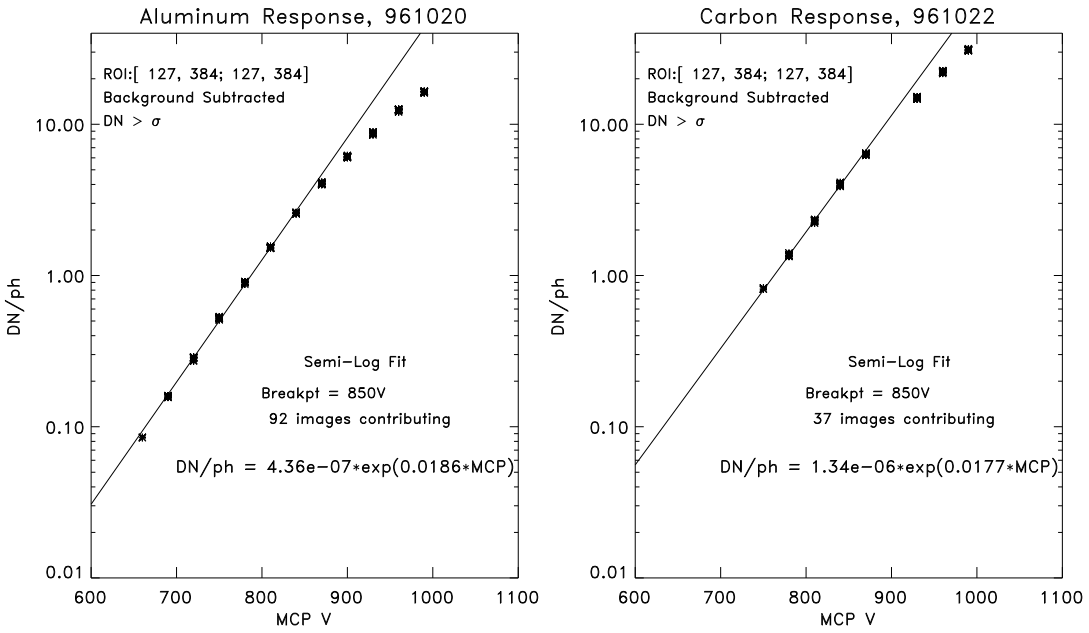

Fig. 8. Exponential (semi-log) fit to data in Fig. 6.

2) Influence of the breakpoint voltage in the fit.

Limiting the fit to MCP < 850V is based upon visual inspection of the data. The sensitivity of the fit to the breakpoint value can be estimated by comparing fit

parameters derived for MCP < 920V instead, again using equal weighting. We find

$$A = 27.53 \pm 1.26\,\mathrm{DN/ph}, \quad B = 13.83 \pm 0.03 \qquad [\mathrm{Al}]$$

$$A = 45.31 \pm 1.68\,\mathrm{DN/ph}, \quad B = 14.08 \pm 0.08 \qquad [\mathrm{C}]$$

These values reflect a somewhat flatter slope for both Al and C, as might be expected, but do not constitute any drastic change in results.

3) ROI.

The size and placement of the ROI on the image may affect the results. (In all the above, we used an image-centered 256×256 ROI.) We investigate two alternate choices to assess these effects.

a) Size of ROI. The analysis was repeated using a smaller, centered 100×100 pixel ROI, the same as that used in the MSFC study. The results, depicted in Fig. 9, fall at the limit of the error bars in the 256×256 ROI fit, and do not suggest any great dependence upon ROI size.

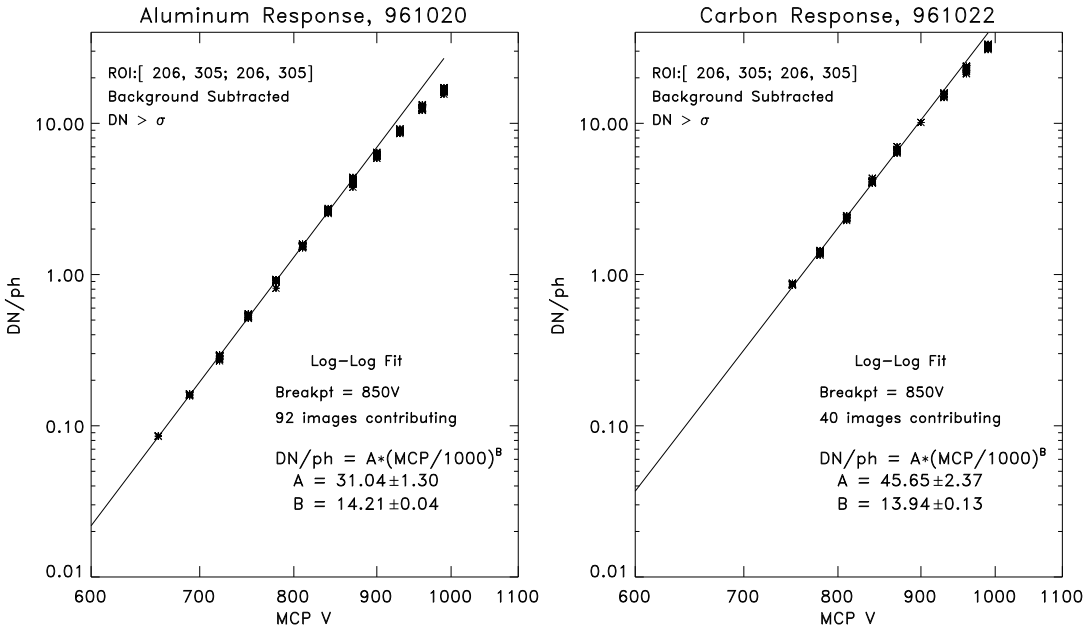

Fig. 9. Response based upon smaller ROI.

b) Location of ROI. The X-ray beam center is known to have been shifted toward the lower right-hand corner of the CCD face during the C tests, and vignetting may therefore affect results for ROIs near image center. An example of smoothed Al and C images giving an impression of the beam offset is presented in Fig. 10. A diagonal cut from the upper left corner to the lower right corner of the two beam patterns, shown in Fig. 11, provides an idea of the magnitude of the variation across the images. The Al beam is well centered and is relatively flat over the central 256 pixels, whereas a clear trend of ∼25% is visible in the C trace.

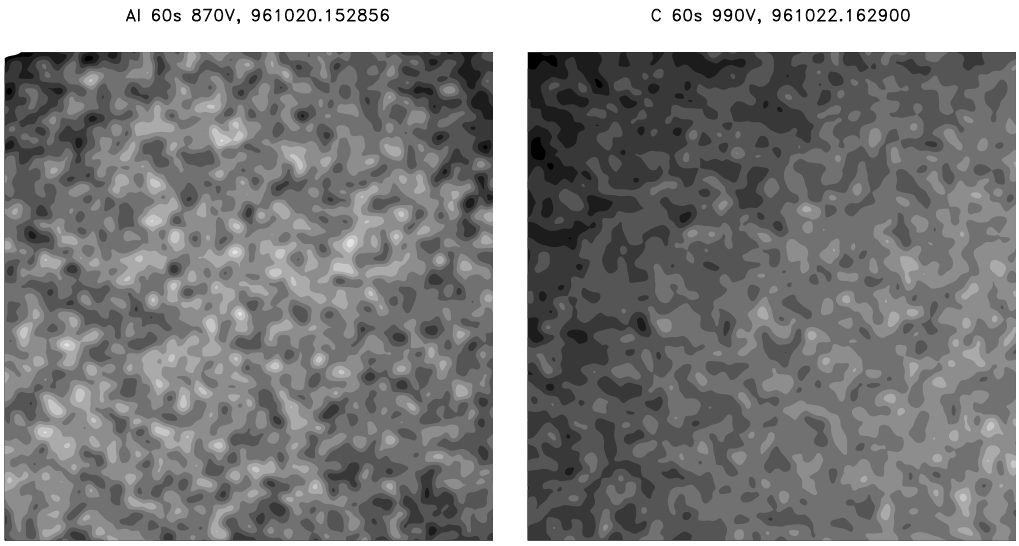

Fig. 10. Smoothed Al and C images showing source beam patterns over entire 512×512 CCD array. Note the apparent vignetting toward the upper left corner of the C image.

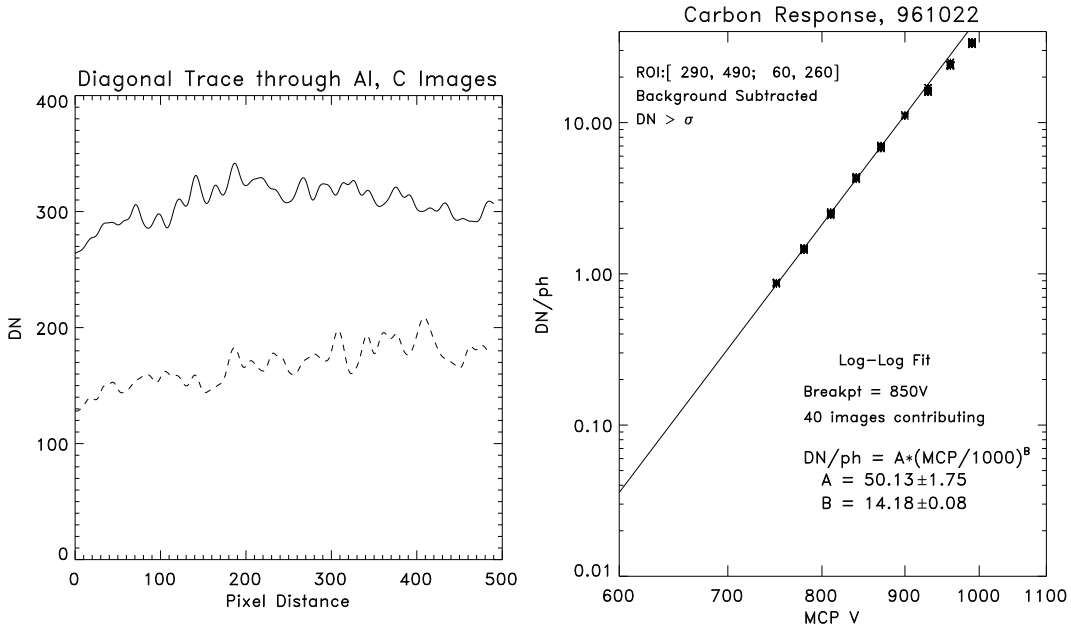

Fig. 11. Diagonal trace from upper right to lower left through Al (solid) and C (dashed) images in Fig. 10. Note the trend across the C image.

Fig. 12. Log-log fit for ROI offset to lower right side of C images.

Fig. 12 shows the detector response fit for Carbon images analyzed with a rectangular ROI offset toward the lower right. The slope B is about the same, but the constant value A is elevated $\sim 7.5\%$. This may be statistically significant and may be indicative of the systematic errors in the derived amplitudes caused

by non-uniform illumination of the detector. Its reality difficult to assess, however, since with the ROI nearer to the edge of the image other effects may come to bear. For example, there is evidence that the lower edge of the CCD may be subject to progressive loss of DN for long integration times (cf. G. D. Berthiaume, "GOES-M Solar X-ray Imager (SXI) Recalibration Report," Project Report NOAA-23, MIT/LL, 1998; V. J. Pizzo, "SXI-M Recalibration Analysis Report: Point-Spread Function," NOAA/SEC, 1999). It is also unclear what effect the beam offset may have had upon the flow meters used to calibrate the absolute flux impinging upon the detector. If the vignetting was introduced by baffles near the X-ray source, then it is conceivable that the flux at the flow meter was reduced proportionately, and that the centered 256×256 ROI remains the more appropriate measure.

4) Actual Voltage versus Requested Voltage

The High Voltage Power Supply (HVPS) was run at ambient room temperatures during the tests. It is known that the actual HVPS 1K output to the MCP differs from the requested Image Control Table (ICT) setting values, and that this difference varies as a function of temperature. The actual voltages reported out to the Electrical Ground Support Equipment (EGSE) were compiled manually by the operators. A scatter plot of actual versus requested tabular values is shown in Fig. 13. The points along the bottom of the graphs (indicating large deviations toward low voltages) result from a readout timing error in the circuitry. For our purposes, it is accurate enough to conclude that the actual voltage output to the MCP was about 1.5% below the requested value. This has the effect of shifting the data in Fig. 6 to higher DN/ph values by a constant amount. We can correct for this effect in the the derived response formulas by multiplying the power-law fit constant "A" (the DN/ph amplitude) by $1.015^{14.2} = 1.24$.

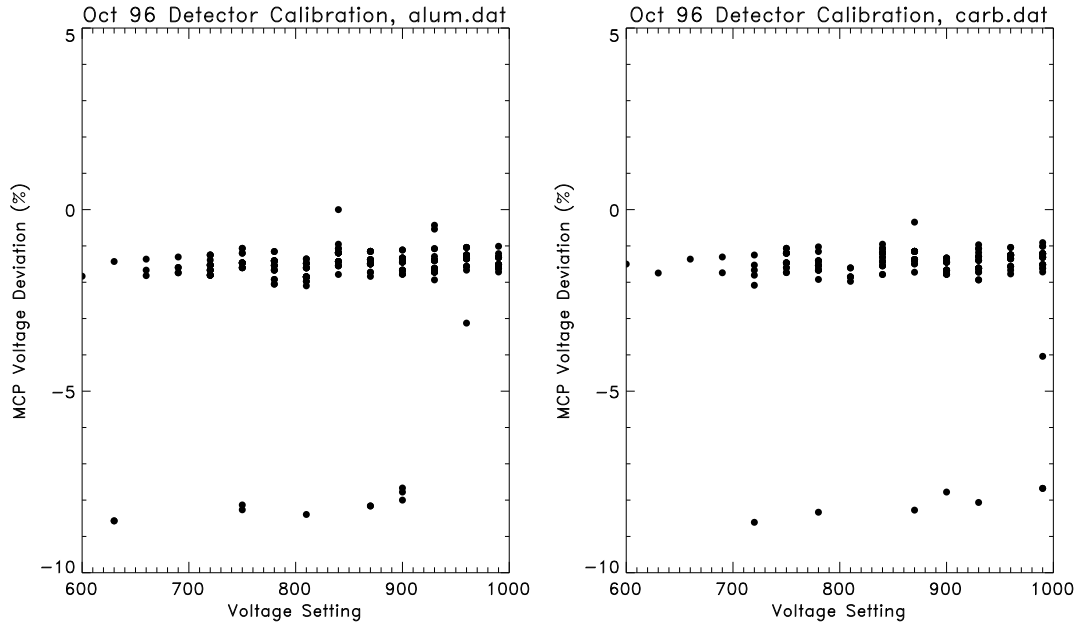

Fig. 13. Actual voltage output by MCP, stated as percentage of requested voltage setting.

5) Detector Saturation Effects

At high photon flux rates, MCP devices typically exhibit saturation effects: so much charge is generated so quickly within the micro channels that the available electron population is depleted and the DN/ph response declines. The deviation (or roll-off) from the log-log response function fits evident above 850V in Fig. 6 appear to be due to detector saturation. At high MCP voltages, the amount of charge in the cascade initiated by the detected photons is very large, and the electron depletion rate in the device is too high to sustain a linear response (in the log-log domain of the response function fit).

We can obtain a better estimate of saturation effects in the SXI detector from Fig. 14. Here we plot in two different ways the deviation of the image data from the fit displayed in Fig. 6. On the left we plot the deviation from the fit in terms of DN/ph response for the image data of Fig. 6; on the right are the same data, but plotted as a fractional deviation from the fit value. Both figures illustrate a marked roll-off above ~850V, with the detector response falling as much as 30-40% below expectations at the highest test voltages.

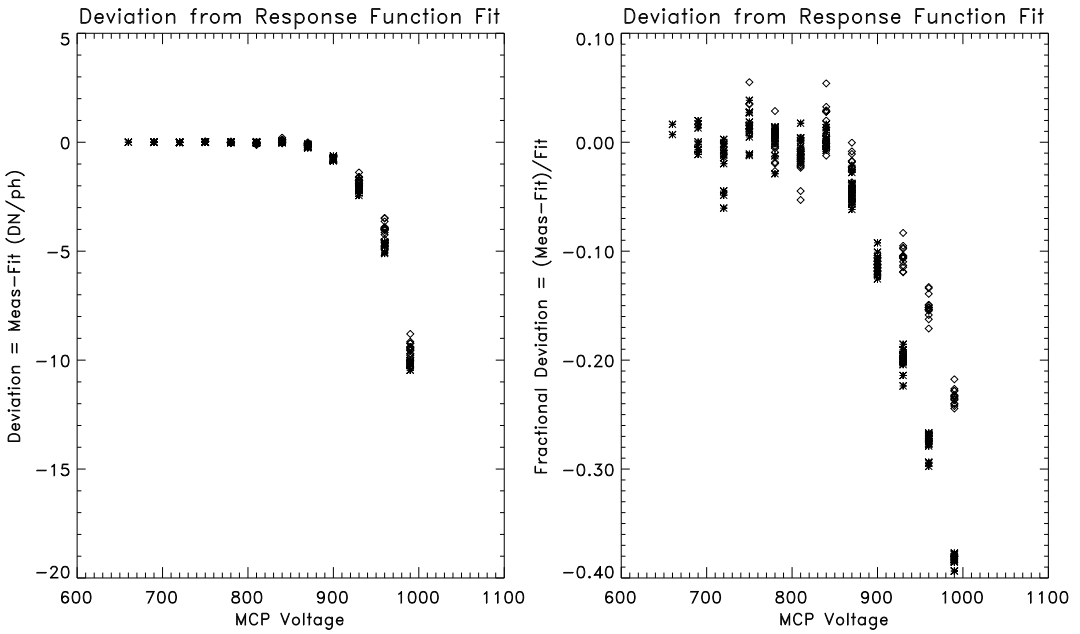

Fig. 14. Deviation of the detector response from the ideal fits associated with the data of Fig. 6. Al data given by asterisks, C by diamonds.

Fig. 14 suggests that the absolute deviations from the fit (DN deficit per photon incident) are roughly the same at the two wavelengths. Hence the fractional deviation appears less for C than for Al at a given voltage, since the quantum efficiency of the detector is greater at long wavelengths (more DN per incident photon).

However, these relationships may be somewhat illusory, since the saturation mechanism depends only in part upon the magnitude of the cascade, which is a function of MCP voltage. The other major factor in the saturation process is the temporal rate at which photons activate the MCP. For the detector tests, the flux of incident photons

was determined (K. Russell and J. Chappell, April 13, 1997) to be approximately 0.1 ph/px/sec for the C source, 1.3 ph/px/sec for the Al source. (These fluxes refer to the nearly uniform beam of photons incident on the face of the MCP detector and are expressed in terms of unit area illuminated on the CCD.) Hence the Al and C tests were run at incident photon flux levels differing by more than an order of magnitude.

Although saturation effects are expected to be proportional to the incident photon flux rate, the response need not be linear. Direct determination of the magnitude and form of this effect is precluded because flux rates were not varied in the course of the detector tests. This limitation may have implications for operational photometry, since detector saturation affects not only the magnitude of the deviation from the fits but also the voltage at which the roll-off occurs. That is, when photon fluxes are very high we can expect saturation effects to become evident at normal operating voltages, down in the 650-800V range.

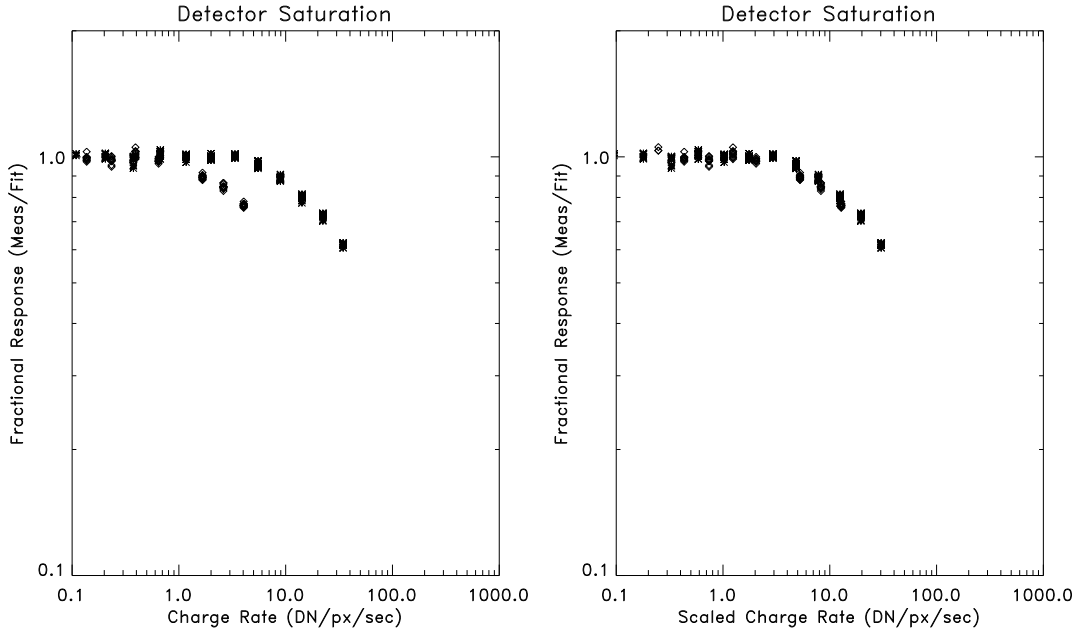

Fig. 15. Fractional response of the detector (relative to ideal fit values) as a function of charge production rate. At left, charge rate is assumed proportional to incident photon flux rate, at right it is scaled as the square root of the incident photon rate.

Given the limitations of the test data, perhaps the best estimate we can make of detector saturation effects is shown in Fig. 15. The idea here is to combine what we know about the detector cascade response (which is a function of MCP voltage) with what little information we have related to photon flux rate. We hypothesize that the fractional response (relative to the ideal fit DN/ph) of the detector can be stated as a function of the charge production rate, which is the product of the known voltage-dependent DN/ph response of the detector and the incident photon flux rate. That is,

$$(\text{charge production rate}) \propto (\text{DN/px/ph} * \text{ph/px/sec}) = \text{DN/sec}$$

In Fig. 15, we plot at left the fractional detector response (the ratio of the measured DN/px/ph to the fit value) as a function of the above product, for the Al and C data of Fig. 14. If saturation losses were directly proportional to the photon flux rate, we would expect the Al and C data to overlap and the roll-off from the fit to occur at the same charge production rate. However, in Fig. 15 (left) it is seen that the data from the C source rolls off at much lower charge rates than for Al, although the decline in response at high charge rates has a similar slope.

For Fig. 15 (right) we have modified the above charge rate expression to read

$$(\text{scaled charge production rate}) \propto (\text{DN/px/ph}) * \sqrt{(\text{ph/px/sec})}$$

That is, we have scaled the charge production rate to the square root of the incident photon flux. The data from the two sources now overlap quite well, and the roll-offs from the fit are consistent.

The assessment of saturation effects given by Fig. 15 (right), square-root scaling for the incident photon rate, is completely ad-hoc and the confidence with which it can be applied is very low. On the other hand, given that there are only two incident photon flux rates to work with, it appears little more can be substantively achieved with the available data.

5. Conclusions

The best characterization of the available detector test data is

$$\text{DN/ph} = (38.0 \pm 1.2) * (\text{MCP}/1000)^{(14.20 \pm 0.02)} \qquad [\text{Al}]$$

$$\text{DN/ph} = (57.8 \pm 2.2) * (\text{MCP}/1000)^{(14.20 \pm 0.12)} \qquad [\text{C}]$$

where MCP refers to the actual (as opposed to requested) MCP voltages. This analysis implicitly takes into account the quantum efficiency of the detector itself, and it reflects the response of the detector as a whole.

For completeness, we note that a slightly different determination of the fit parameters has been published in the Berthiaume SXI Recalibration Report previously referenced. The same data were used in the fit, but statistical weighting was applied. From his Table 9, we have

$$\text{DN/ph} = (38.3 \pm 0.32) * (\text{MCP}/1000)^{(14.11 \pm 0.00039)} \qquad [\text{Al}]$$

$$\text{DN/ph} = (55.6 \pm 0.98) * (\text{MCP}/1000)^{(14.11 \pm 0.00098)} \qquad [\text{C}]$$

Requested MCP voltages are used in these relations.

Direct comparison of our results with reported MSFC values cannot be undertaken until corrections for certain processing errors in their Integrated Sensitivity analysis (Jon Chappell, private communication) are completed.

From an operational standpoint, the lack of calibration data over a range of incident photon flux levels makes it impossible to assess saturation effects with any confidence. This poses a major impediment to accurate photometry of intense solar

sources. It may be possible to obtain better estimates of these effects during on-orbit operations through cross-calibration with other instrumentation, such as HXRS.

In computing the total system throughput, the above results must be convolved with the full wavelength dependence of the detector. One way to approach this for SXI-M is to normalize the anticipated detector wavelength curve originally supplied by MSFC such that the response at Carbon is 1.0, and use the above formula for Carbon to set the absolute value (Fig. 16). That is, to obtain the integrated DN/photon at some specified actual MCP voltage, we multiply the above Carbon response formula by the fractional response value for that wavelength as given in Fig. 16.

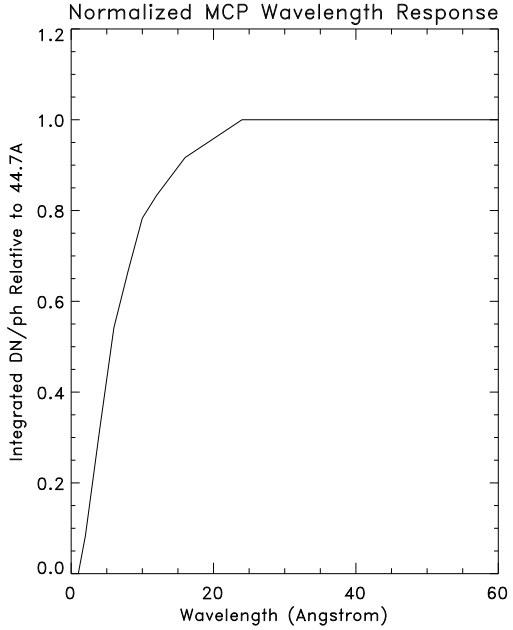

Fig. 16. Relative response of the MCP as a function of wavelength.

Finally, the elevated Carbon response noted in conjunction with Fig. 12 (ROI offset from image center) may be real, but would be a minor correction to the overall throughput when all other sources of error are considered. For example, the absolute accuracy of the input photon count as measured by the flow meter (I_p) is not well determined, and is subject to many sources of error. In addition, variations in response due to ageing of the MCP and other optical elements, saturation and thermal effects, etc, will certainly be at least of the order of the 7.5% uncertainty associated with the detector response characterization.

6. Acknowledgements

Very helpful comments by Pat Bornmann and Greg Berthiaume on drafts of this report are gratefully acknowledged.

GUIDE TO APPENDIX 1 and 2

The two tables of reduced data that follow form the basis for the sensitivity analysis. The first set refers to images with the aluminum source, the second to the carbon source. Both datasets pertain to the analysis conducted with the ROI defined as the central 256×256 pixel area of the CCD.

In each case, the first line indicates the data directory accessed, and the pixel locations specifying the dimensions of the ROI are given as [x0,x1,y0,y1].

The column headings are as follows:

`hex`:	The last 6 hex digits of the image ID
`dec`:	The hex ID decimal equivalent used in the sxi0 archive files
`mcp`:	The requested MCP voltage setting (volts)
`int`:	The exposure integration time (sec)
`spm_id`:	The flow meter record ID
`pha_cts`:	The total counts in the flow meter record
`CDN`:	The average DN in the ROI, corrected for background
`SDN`:	The standard deviation of the CDN
`I_p`:	The number of photons per pixel incident on the detector during the exposure, from the flow meter data
`RawDN`:	The raw average DN in the ROI (NO background correction)

The first grouping of reduced data refers to the images used for the background determination. For the background images, only the raw DN are given. For the carbon data, only the four exposures taken at the end of the test run are listed up front; additional background exposures (which were not used in the final analysis, since the test system was judged to be out of equilibrium at the time those exposures were taken) are listed at the end of the printout.

The line beginning "background fit" gives the linear fit coefficients C_1 and C_2 to the background, followed by the standard deviations of those coefficients.

Finally, the results for each image used in the analysis are listed.